JOURNAL OF AIRCRAFT
Vol. 47, No. 4, July–August 2010

Improving the Aerodynamic Performance of Micro-Air-Vehicle-Scale Cycloidal Rotor: An Experimental Approach

Moble Benedict,* Manikandan Ramasamy,† and Inderjit Chopra‡
University of Maryland, College Park, Maryland 20742

DOI: 10.2514/1.45791

Performance and flowfield measurements were conducted on a small-scale cyclorotor for application to a micro air vehicle. Detailed parametric studies were conducted to determine the effects of the number of blades, rotational speed, and blade pitching amplitude. The results showed that power loading and rotor efficiency increased when using more blades; this observation was found over a wide range of blade pitching amplitudes. The results also showed that operating the cyclorotor at higher pitching amplitudes resulted in improved performance, independently of the number of blades. A momentum balance performed using the flowfield measurements helped to quantify the vertical and sideward forces produced by the cyclorotor; these results correlated well with the force measurements made using load balance. Increasing the number of blades increased the inclination of the resultant thrust vector with respect to the vertical because of the increasing contribution of the sideward force. The profile drag coefficient of the blade sections computed using a momentum deficit approach correlated well with typical values at these low chord Reynolds numbers. Particle image velocimetry measurements made inside the cage of the cyclorotor showed that there are rotational flows that, when combined with the influence of the upper wake on the lower half of the rotor, explain the relatively low efficiency of the cyclorotor.

Nomenclature

A	=	cycloidal-rotor rectangular projected area, $2bR$, m^2
b	=	blade span, m
C_P	=	rotor power coefficient, $P/\rho A(\Omega R)^3$
C_T	=	rotor thrust coefficient, $T_{\text{Res}}/\rho A(\Omega R)^2$
c	=	blade chord, m
c_d	=	drag coefficient
c_l	=	lift coefficient
D	=	rotor blade sectional drag/unit span, N m^{-1}
DL	=	disk loading, T_{Res}/A, N m^{-2}
FM	=	figure of merit, $P_{\text{ideal}}/P_{\text{meas}}$
$\dot{m}$	=	mass flow rate per unit span, kg m^{-1} s^{-1}
N_b	=	number of blades
P	=	total aerodynamic power, W
PL	=	power loading, T_{Res}/P, N W^{-1}
P_{ideal}	=	ideal power, W
P_{meas}	=	measured power, W
P_Y	=	momentum of the fluid per unit span in Y direction, kg s^{-1}
P_Z	=	momentum of the fluid per unit span in Z direction, kg s^{-1}
R	=	radius of the rotor, m
T_{Res}	=	resultant thrust, N
T_Y	=	rotor sideward thrust, N
T_Z	=	rotor vertical thrust, N
U_T	=	blade tangential velocity, m s^{-1}
V	=	resultant fluid velocity, m s^{-1}
v, w	=	velocity along the Y, and Z directions, m s^{-1}
X, Y, Z	=	rotor coordinate system, m
α	=	blade angle of attack, deg
ζ	=	wake age, deg
θ	=	blade pitch angle, deg
ρ	=	air density, kg m^{-3}
σ	=	rotor solidity, $N_b c/2\pi R$
ϕ	=	phase angle of the resultant thrust vector, deg
Ψ	=	azimuthal position of the blade, deg
Ω	=	rotational speed of the rotor, rad s^{-1}

Received 3 June 2009; revision received 19 March 2010; accepted for publication 19 March 2010.

*Graduate Research Assistant, Department of Aerospace Engineering. Student Member AIAA.

†Assistant Research Scientist, Department of Aerospace Engineering; currently Aeroflightdynamics Directorate, NASA Ames Research Center, Mountain View, CA. Member AIAA.

‡Alfred Gessow Professor and Director, Alfred Gessow Rotorcraft Center, Department of Aerospace Engineering. Fellow AIAA.

Introduction

IN RECENT years, interest has been growing in the use of micro-air-vehicles (MAVs). As the battlegrounds of the future move to restricted, highly populated, urban environments, MAVs can be extremely useful assets to the military. MAVs can also be used for civilian applications such as biochemical sensing, traffic monitoring, border surveillance, fire and rescue operations, wildlife surveys, power-line inspection, and real-estate aerial photography, just to name a few. Several fixed-wing MAVs have already been successfully tested [1–5]. Even though fixed-wing MAVs may be the best performers today in terms of the imposed size and weight constraints, they lack the ability to hover or to operate in highly constrained environments. The latter attributes are important for many missions, not just surveillance. Therefore, the development of efficient hovering rotary-wing concepts will lead to more versatile and useful MAVs with expanded flight envelopes.

To this end, several hovering-capable MAVs based on single main rotor or coaxial rotor configurations have been successfully built and flight-tested [6,7]. However, these MAVs operate in the blade chord Reynolds number range from 10,000 to 60,000 and so they suffer from the aerodynamic inefficiencies of small scale. In fact, most MAVs based on conventional rotors have shown relatively low performance; e.g., the maximum figure of merit achieved to date is only about 0.65 [6]. This implies that scaling down full-scale concepts may not be the correct approach for operating in a completely different aerodynamic regime. Therefore, it is important to investigate alternate solutions such as cycloidal rotors, flapping wings, etc., because they may have potential for better performance at these low Reynolds numbers.

An MAV concept based on a cycloidal-rotor (cyclorotor) system has been proposed as an alternative to a conventional rotor. A cyclorotor (also known as a cyclocopter or cyclogiro) is a rotating-wing system (Fig. 1) in which the span of the blades runs parallel to

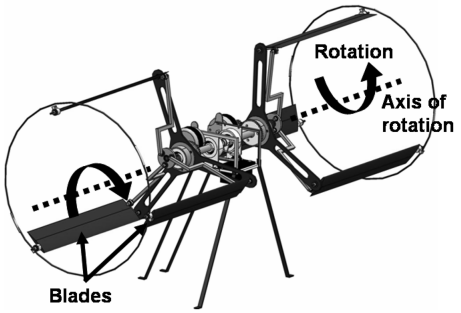

Fig. 1 Cyclorotor MAV.

the axis of its rotation. The pitch angle of each blade is varied cyclically by mechanical means such that the blades experiences positive angles of attack at the top and bottom positions of its trajectory (Fig. 2). The resulting time-varying lift and drag forces produced by each blade can be resolved into the vertical and horizontal directions, as shown in Fig. 2. Varying the amplitude and phase of the cyclic blade pitch can be used to change the magnitude and direction of the net thrust vector produced by the cyclorotor.

Compared to a conventional rotor, each spanwise blade element of a cyclorotor operates at similar aerodynamic conditions (i.e., at similar flow velocities, Reynolds numbers, and angles of attack), and so the blades can be more easily optimized to achieve best aerodynamic efficiency, at least in principle. Moreover, because the blades are cyclically pitched once per revolution (1/rev), unsteady flow mechanisms may delay blade stall onset and so augment the net lift produced by the blades. Prior experiments have suggested that cyclorotors can reach efficiencies comparable to conventional rotor systems [8] and possibly higher values of maximum thrust. Furthermore, because the thrust vector of a cyclorotor can be almost instantaneously set to any direction perpendicular to the rotational axis, compared to a conventional rotor system a cyclorotor-based MAV may ultimately show better maneuverability and agility, which are particularly important attributes for constrained indoor flight operations.

Most of the previous experiments on cyclorotors have been performed at relatively larger scales [8–22]. The key conclusions from these studies are summarized in [23]. Recent tests on a 6-in.-diam three-bladed cyclorotor at the University of Maryland indicated that this concept is promising at the lower Reynolds numbers at which MAVs operate [23–25]. Experimental studies were conducted by varying the rotational speed, blade airfoil profile and blade flexibility in an attempt to optimize the performance of the cyclorotor. This previous study was performed using three blades. However, the study showed that the power loading values obtained for the cycloidal microscale rotor were considerably lower than for conventional helicopter-based microrotors.

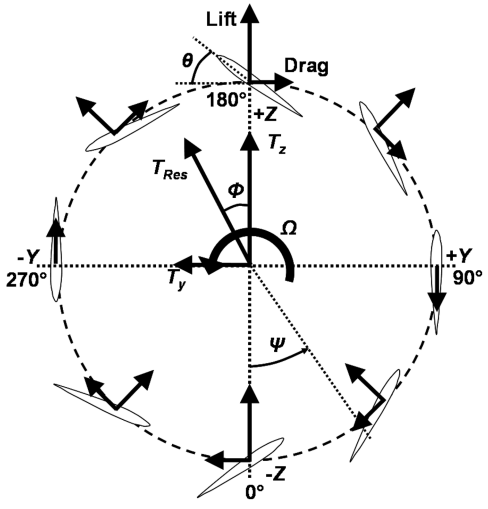

Fig. 2 Cyclorotor blade kinematics and thrust vectors.

Improving the aerodynamic performance of a cyclorotor that vaults a laboratory model to a successfully working hover-capable vehicle depends on developing a fundamental knowledge of its flowfield. The current status of the aerodynamic understanding of the cyclorotor can be rated as qualitative, at best. Many aspects of the flow are still not completely understood. For example, the reason behind the observed absence of blade stall, even when the collective pitch of the blade is set to high values, or the reason for the skewed nature of the rotor wake [23], are not completely understood. In the present study, flowfield measurements were made inside the rotor-cage to better understand the aerodynamics.

The focus of the present work is to perform a parametric study towards understanding the effects of number of blades (that were operated at different blade pitching amplitudes) on the aerodynamic performance of a model-scale cyclorotor. The goal is to use both performance and flowfield measurements to identify an optimum geometric configuration and operating condition(s) at which the cyclorotor operates at best efficiency. It should be understood that the present work is a continuation of the previous work reported in [23], where the authors studied the effect of blade airfoil section, blade flexibility, etc., on the aerodynamic performance.

Performance Studies

Experimental Setup

The experiments were conducted on two-, three-, four-, and five-bladed cyclorotors. A four-bladed cyclorotor is shown in Fig. 3. All the rotors had a diameter and blade span of 0.152 m (0.5 ft). The blades had a uniform chord of 0.0254 m (0.0833 ft) and used the NACA 0010 airfoil section. Details on the design of the cyclorotors are given in [23].

A test rig was built to measure the thrust, torque, and rotational speed of the cyclorotor. A Hall-effect sensor was used to generate a 1/rev signal to measure the rotational speed of the rotor. The power consumption was determined from torque and rotational speed measurements. A range of tests were performed to characterize the performance of the various cyclorotors. Measurements were obtained for all the cyclorotors at blade pitching amplitudes of 25, 30, 35, and 40°, and for rotational speeds ranging from 400 to 2000 rpm.

Particle Image Velocimetry Setup

The particle image velocimetry (PIV) setup is explained in Fig. 4. The PIV hardware included a pulsed dual Nd:YAG laser that was operated in phase synchronization with the cyclorotor. An articulated optical arm was used to locate the light sheet in the required region of interest in the flow. The laser system was capable of being pulsed at frequencies up to 15 Hz, and was synchronized to the rotational frequency using the 1/rev trigger and a phase-locking master timing control unit.

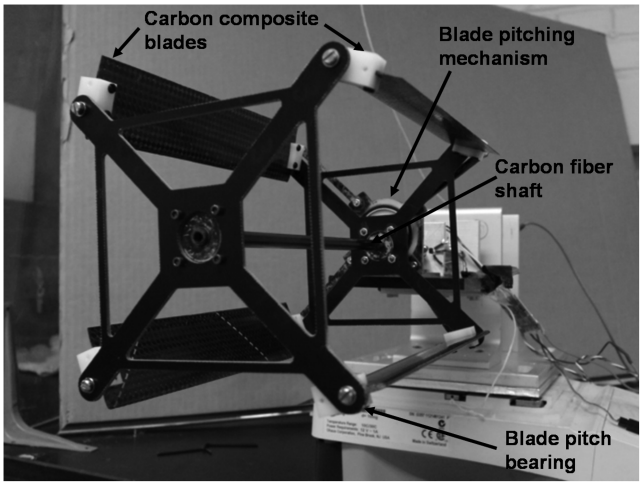

Fig. 3 Four-bladed cyclorotor.

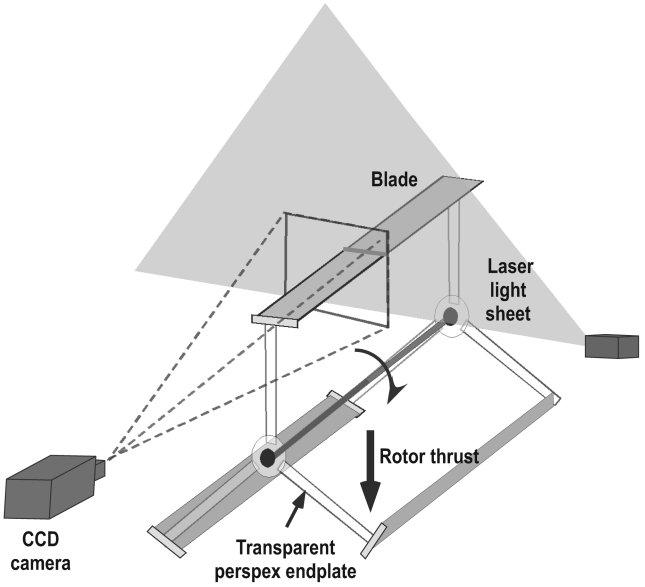

Fig. 4 Schematic of the PIV setup.

Before each sequence of measurements the entire test area was seeded uniformly with a fog of submicron mineral oil particles. The PIV technique measures the flow velocity of these seed particles, so it is essential to use small particles to prevent tracking errors but the particles must also be large enough to produce sufficient Mie scattering of the laser light. The flow images were acquired using a 2-megapixel-resolution digital camera, which was placed orthogonal to the laser sheet. The dual lasers were fired with a pulse separation time of 10 μs. A high-speed digital frame grabber was used to acquire the resulting image pairs for analysis. For the PIV image processing, a recursive technique called a deformation-grid correlation algorithm was applied to the images [26], which has been shown to be better for measuring the high-velocity gradients found inside rotor wake flows [27].

The PIV setup was used to study the flowfield inside the cage of cyclorotor as well as in the wake below it. To obtain the chordwise flow velocities the laser sheet was placed at the midspan of the rotor perpendicular to the blade span (Fig. 4). It was extremely challenging to obtain good PIV measurements inside the cyclorotor, because the end plates blocked optical access and also because of the shadows cast by the individual blades. To help minimize the problem, new rotor endplates were made out of transparent Plexiglas. The PIV measurements were made only on the two- and four-bladed cyclorotors.

Results and Discussion

Performance Results

Rotor Forces

The coordinate system used for the cyclorotor is shown in Fig. 2. The azimuthal position of the blade, Ψ, is measured counterclockwise from the negative Z axis. The blade pitch angle θ is measured tangentially to the circular path of the blade. Intuitively, it appears that with this kind of blade kinematics (discussed in [23]), the rotor should only produce a vertical force T_z. However, the experiments showed that the cyclorotor also produced a sideward force T_y with a magnitude that was comparable to that of the vertical force (Fig. 2). This result was later confirmed by the PIV studies, which showed the presence of a skewed wake system.

The present experimental rig was made in such a way that it could measure both the vertical and sideward force components [23]. The resultant thrust T_{Res} is obtained from the measured T_z and T_y using

$$T_{\text{Res}} = \sqrt{T_z^2 + T_y^2} \tag{1}$$

The angle made by the resultant thrust T_{Res} with the vertical ϕ is then given by

$$\phi = \tan^{-1}\left(\frac{T_y}{T_z}\right) \tag{2}$$

Figure 2 shows a schematic of the forces produced by the rotor. Figures 5 and 6, respectively, show the variation of nondimensional vertical and sideward forces produced per blade, C_{T_z}/σ and C_{T_y}/σ, with rotational speed for two-, three-, four-, and five-bladed cyclorotors at a pitching amplitude of 40°. The vertical component, C_{T_z}, remained almost constant with rotational speed, while the sideward component, C_{T_y} increased steadily with the rotational speed. Another significant observation from these tests was that increasing the number of blades tends to increase the phase angle of the resultant thrust vector (ϕ). This is primarily because the contribution of the sideward force to the total force increases as the number of blades increases. In the remainder of this paper, the thrust refers to the resultant thrust (i.e., to T_{Res}).

The total power required for the rotor was obtained from the torque and rotational speed measurements. Tare tests were carried out at different rotational speeds after removing the blades to measure the profile power consumed by the rest of the rotor structure other than the blades and also the balance associated losses; this constituted only around 10–15% of the total power. These results were then subtracted from the total power measurements to obtain the aerodynamic power required to rotate the blades. Blade aerodynamic power includes the induced power, profile power, rotational losses, power loss from interference effects, and the aerodynamic power required for pitching the blades.

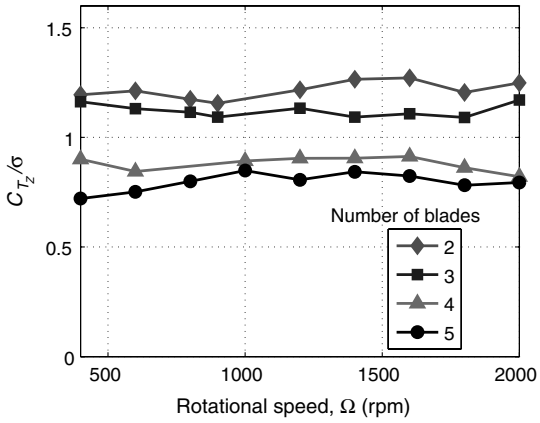

Fig. 5 Nondimensional vertical force C_{T_z}/σ versus rotational speed (rpm) for two-, three-, four-, and five-bladed cyclorotors at 40° blade pitching amplitude.

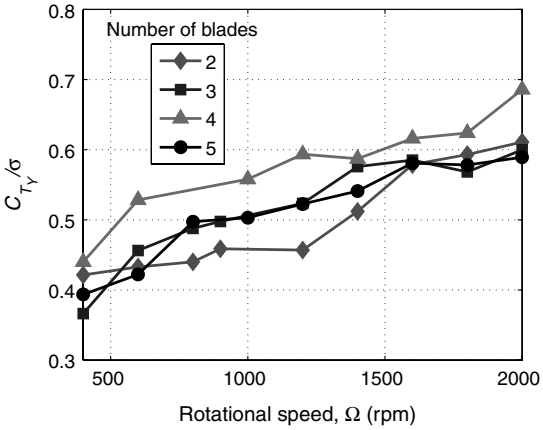

Fig. 6 Nondimensional sideward force C_{T_Y}/σ versus rotational speed (rpm) for two-, three-, four-, and five-bladed cyclorotors at 40° blade pitching amplitude.

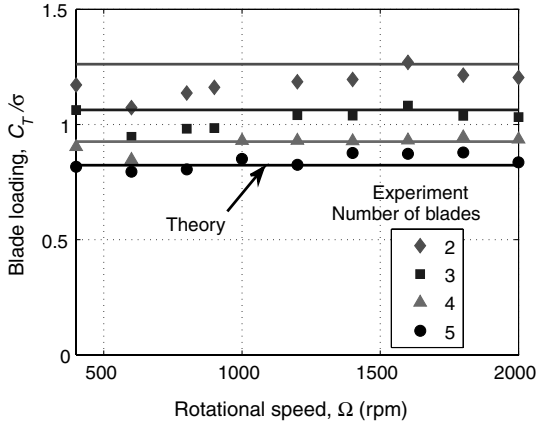

Fig. 7 Nondimensional resultant thrust C_T/σ versus rotational speed (rpm) for two-, three-, four-, and five-bladed cyclorotors at 35° blade pitching amplitude.

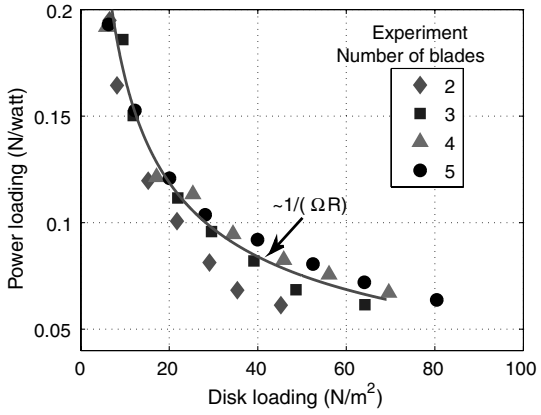

Fig. 9 Power loading versus disk loading for two-, three-, four-, and five-bladed cyclorotors at 40° blade pitching amplitude.

Thrust and Aerodynamic Power Measurements

Figures 7 and 8, respectively, show the variation of nondimensional resultant thrust (C_T/σ) and power (C_P/σ) per blade with rotational speed for two-, three-, four-, and five-bladed cyclorotors at a pitching amplitude of 35°. As expected, C_T/σ and C_P/σ remains constant with rotational speed since the thrust and power varies as the square and cube of rotational speed, respectively.

In Fig. 7, the experimentally measured thrust values are compared with predictions that were obtained using a quasi-steady aerodynamic model based on blade element momentum theory and a uniform inflow model based on the rectangular projected area A [24]. The inflow model also includes the effect of the wake from the upper half of the cyclorotor on the lower half of the rotor. In all the cases, the thrust predictions were found to be within 10–15% of the measured values. From Fig. 7, it can be seen that the two-bladed rotor has the maximum thrust per blade, followed by the three-, four-, and five-bladed rotors. This is because the total thrust increases with the number of blades, which increases the inflow and thereby reduces the effective angle of attack of each of the blades. The aerodynamic model also captures this effect. The performance of the cyclorotors can also be affected by the interference between the blades, which is an effect that increases with the number of blades. However, these interference effects are not presently included in the modeling. Again, as in the case of the thrust, the power consumed per blade (Fig. 8) for the different cyclorotors tested is not the same because of the changes in the inflow and blade-on-blade interference effects.

Power Loading

Figure 9 shows the variation of power loading (thrust/power) with disk loading (T_{Res}/A) for different cyclorotors (two-, three-, four-, and five-bladed) at the 40° pitching amplitude. As shown, the power loading varies as $(\Omega R)^{-1}$, because thrust is a function of the square of rotational speed and power varies as the cube of the rotational speed.

Figures 9–12 show the variation of the measured aerodynamic power loading with disk loading for the two-, three-, four-, and five-bladed cyclorotors. Each figure shows the results for different pitching amplitude. Varying the rotational speed changed the rotor thrust level. Also, it should be noted that the disk loading is proportional to the total thrust produced by the cyclorotor, because all the rotors tested in the present study had the same actuator area A.

From the results in Fig. 10, it can be seen that at 25° blade pitching amplitude the four-bladed cyclorotor has the best power loading for all values of disk loading, followed by the five-, three-, and two-bladed rotors. The power loadings of the two- and three-bladed cyclorotors were found to be comparable; however, they were still significantly lower than that found for the four- and five-bladed rotors.

For the 30° pitching amplitude case (Fig. 11), the power loadings produced by four- and five-bladed cyclorotors were comparable at higher disk loading values. However, at lower disk loading values the four-bladed rotor produced better power loading than five-bladed rotor. At all the disk loadings, the three-bladed cyclorotor was inferior to both the four- and five-bladed rotors. The two-bladed rotor produced the lowest power loading.

For the 35° pitching amplitude (Fig. 12), the five-bladed cyclorotor performed better than all of the other rotors, followed by the four-bladed, three-bladed, and two-bladed rotors. However, it was interesting to note that for disk loading values less than 25 Nm^{-2}, the two-bladed rotor actually performed better than the three-bladed rotor. For the 40° pitching amplitude case (Fig. 9), the results showed the superior performance of the five-bladed rotor over the four-, three-, and two-bladed rotors.

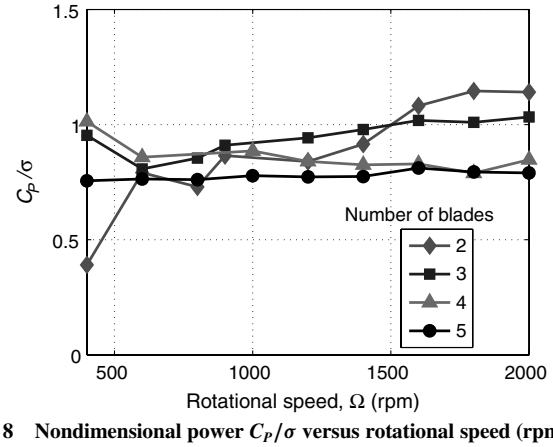

Fig. 8 Nondimensional power C_P/σ versus rotational speed (rpm) for two-, three-, four-, and five-bladed cyclorotors at 35° blade pitching amplitude.

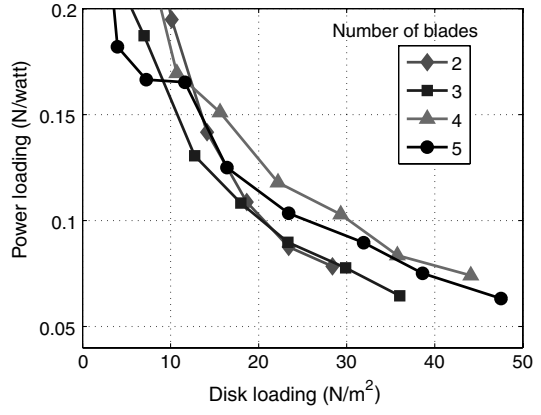

Fig. 10 Power loading versus disk loading for two-, three-, four-, and five-bladed cyclorotors at 25° blade pitching amplitude.

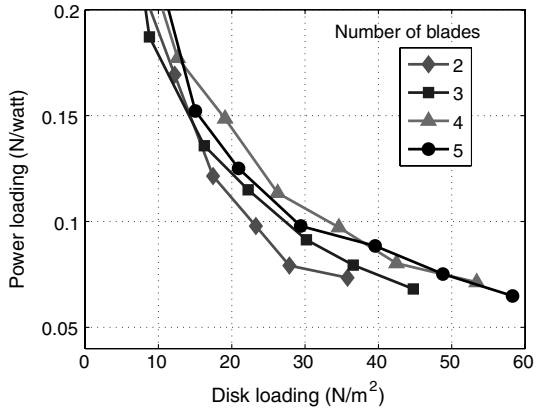

Fig. 11 Power loading versus disk loading for two-, three-, four-, and five-bladed cyclorotors at 30° blade pitching amplitude.

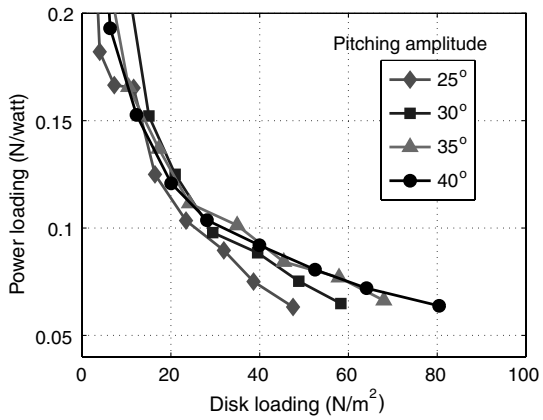

Fig. 13 Power loading versus disk loading for five-bladed cyclorotor at different blade pitching amplitudes.

Figures 9–12 show that the rotor with higher number of blades (higher solidity) produced the better power loading for the same value of disk loading (or thrust). This may be because of the fact that a rotor with higher solidity can achieve a given value of thrust at a lower rotational speed compared to a rotor with a lower solidity. The associated reduction in profile power due to the operation at a lower rational speed must have outweighed the increase in profile power due to the increase in solidity. This trend remained consistent across a wide range of blade pitching amplitudes.

The foregoing results do not prove that more blades is a more desirable design; it only shows that power loading improves with solidity until around 0.21 is reached (four-bladed rotor), beyond which there was only a marginal improvement. The trends observed in the above results are a combined effect of both number of blades and solidity. To isolate the effect of number of blades, rotors with different number of blades would have to be tested at the same solidity by varying the chord length of the blades used on each rotor. However, this work is beyond the scope of this paper.

Figure 13 shows the variation of the power loading with disk loading for a five-bladed cyclorotor at different blade pitching amplitudes. It was observed that the best power loading and maximum thrust was obtained with the 40° pitching amplitude for all the cyclorotors tested. In all of these cases, the thrust increased linearly from 25 to 40° pitching amplitude showing no sign of blade stall. Power increases relatively slowly with blade pitch, clearly indicating that stall does not occur on the blades. It is significant to note that the blades were not stalling at such high pitch angles. Furthermore, from the PIV studies it was seen that the induced velocities in the rotor wake were relatively high, and were comparable to the blade velocity itself. Therefore, even though the geometric angle of attack was 40°, the high induced velocities kept the angles of attack below the stall values. Previous PIV studies [23] also showed the presence of a dynamic stall vortex at the leading edge of the blade and flow reattachment at a pitch angle of 40°. The delay of the stall to higher pitch angles (a known mechanism associated with dynamic stall) may occur because of the 1/rev pitching oscillation of the blades.

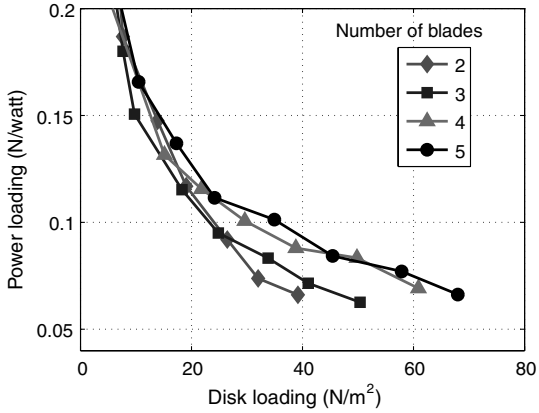

Fig. 12 Power loading versus disk loading for two-, three-, four-, and five-bladed cyclorotors at 35° blade pitching amplitude.

PIV Results

Flow Inside the Cyclorotor

It is important to measure the flowfield inside the cyclorotor to understand the mechanism of lift production as well as to explain some of the observations made during the performance study, such as the production of a sideward force (Fig. 2) and the absence of blade stall at high angles of attack. Flowfield measurements can also expose an understanding of the efficiency of such a system based on the uniformity (or otherwise) of the inflow. The flow model used in the present analysis was based on a uniform inflow assumption. Obtaining an understanding of the flow inside the rotor can be useful in developing a better inflow assumption for the model, which will help in predicting the thrust and power more accurately.

The PIV system (Fig. 4) was used to obtain the velocity measurements in the plane of the rotor and perpendicular to the blade span. The measurements were made on the two-bladed and four-bladed cyclorotors, the results being shown in Figs. 14–18. Figures 14–17 show the phase-averaged velocity vectors (resultant velocity) inside and around the two-bladed rotor at four different wake ages: namely, 0, 30, 120, and 150°. A wake age of 0° corresponds to the alignment of the laser light sheet with the trailing

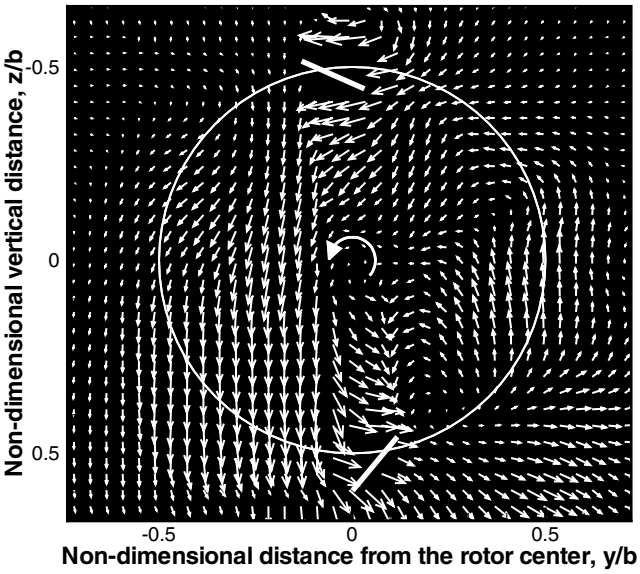

Fig. 14 PIV measurements showing the flowfield inside the two-bladed cyclorotor; wake age $\zeta = 0°$.

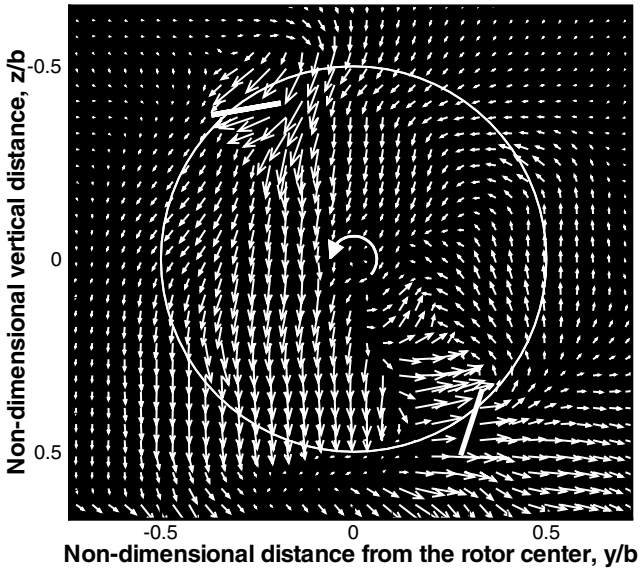

Fig. 15 PIV measurements showing the flowfield inside the two-bladed cyclorotor; wake age $\zeta = 30°$.

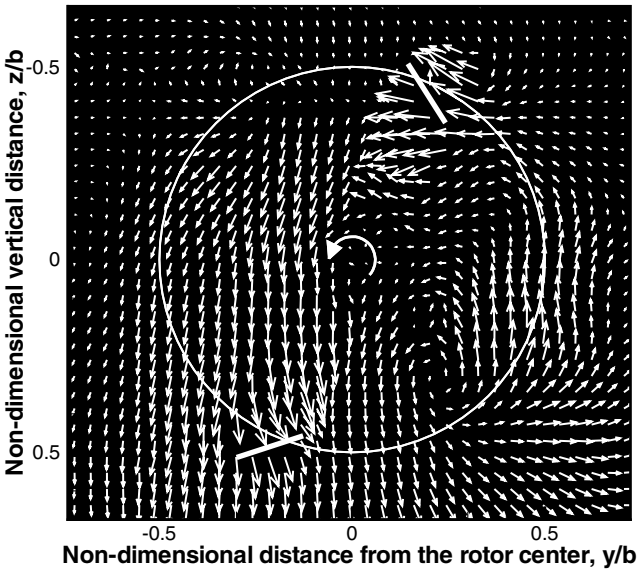

Fig. 17 PIV measurements showing the flowfield inside the two-bladed cyclorotor; wake age $\zeta = 150°$.

edge of the blade when the blade reaches the lowest point in its cycle. Because there are two blades, the flow structures are repeated after 180°. The length of the vectors shows the magnitude of the resultant velocity. Spurious vectors that were produced by reflections from the blades were all removed.

Flowfield measurements for the four-bladed case were performed for wake ages of 0, 20, 40, 60, 75, and 90°. For the four-bladed rotor, the flow repeats after 90°. Figure 18 shows the time-averaged flowfield of all these cases. In these figures, the distances are nondimensionalized by the blade span and the velocity is normalized by blade velocity. The key observation from the PIV measurements is the large region of rotational flow inside the rotor. This result, coupled with the fact that the lower half of the rotor is operating in the wake of the upper rotor, can account for some of the energy loss and can explain the lower efficiency of the present cyclorotors when compared to a conventional rotor system.

The rotational flow also creates an asymmetry of the inflow about the Z axis, as can be seen in Figs. 14–18 (skewed wake structure), which is consistent with the sideward force measured during the performance tests. The relative complexity of the flow inside the rotor-cage also emphasizes the need for a more detailed inflow model or for a computational fluid dynamics based model to capture the flow physics and accurately predict the performance of a cyclorotor.

An important observation here, is the relatively high induced velocities found in the wake; the induced velocities were approximately 60 to 70% of the rotational velocity of the blade section. This inflow will keep the blades operating at lower angles of attack and might explain why the blades do not stall even at high pitch angles.

Thrust from Momentum Balance

The thrust produced by the cyclorotor can also be obtained by computing the change in momentum of the flow passing through a control volume surrounding the rotor. For the present study, a rectangular control volume was used and the net vertical and sideward thrust components were measured from the total momentum flux flowing into the control volume compared to the total momentum flux flowing out. However, the size of the control volume has to be large enough to capture the momentum change in the entire flowfield.

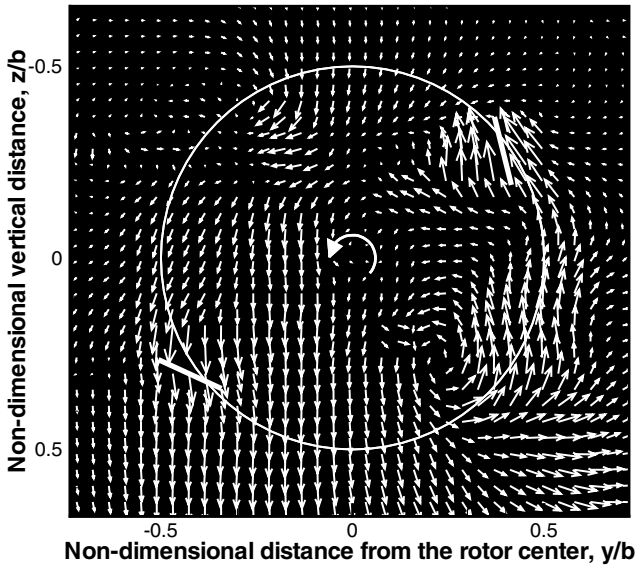

Fig. 16 PIV measurements showing the flowfield inside the two-bladed cyclorotor; wake age $\zeta = 120°$.

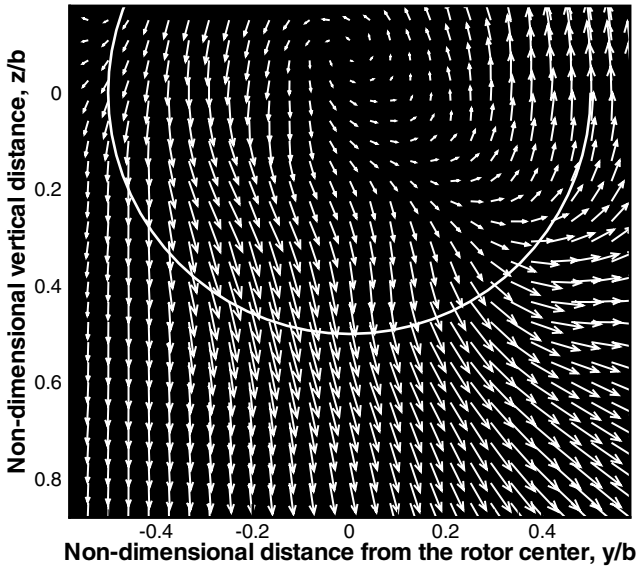

Fig. 18 Time-averaged velocity measurements showing the flowfield inside the four-bladed cyclorotor.

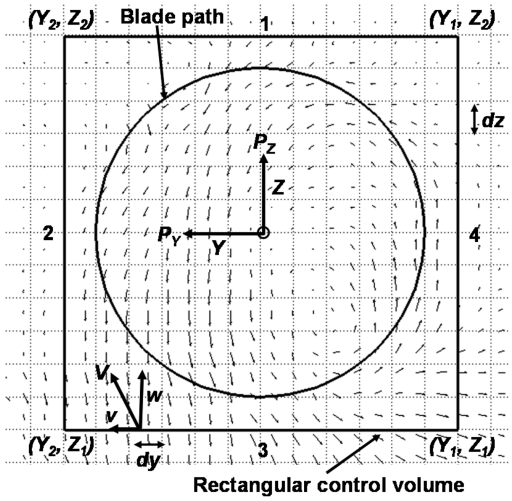

Fig. 19 Schematic showing the procedure used to obtain sectional thrust from a momentum balance at a given spanwise location.

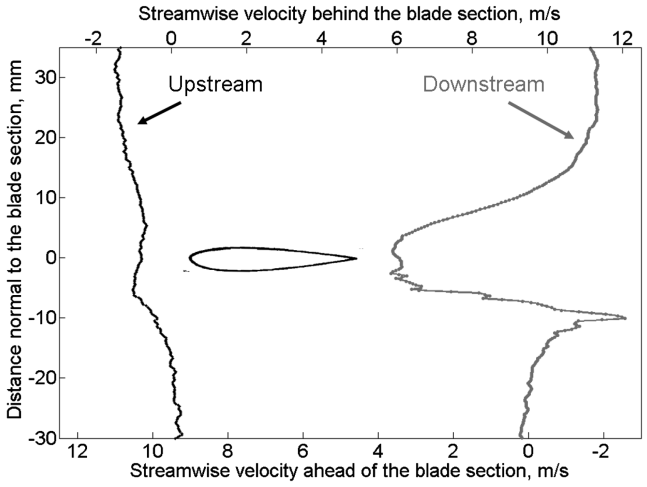

Fig. 20 Velocity deficit behind the cyclorotor blade at the midspan location at 0° azimuthal location.

The schematic in Fig. 19 shows the procedure used for this computation. The first rectangular loop completely encloses the rotor; i.e., the circular blade path of the rotor is within the loop. In the second step, the length of the rectangular loop was increased by Δx (one node in the PIV grid) on all four sides. Subsequent loops increased their length by Δx on all four sides relative to the previous loop. This procedure was continued until the thrust values were converged. The net vertical and sideward thrusts were obtained by numerically evaluating the momentum change across all four sides of the rectangular loop using the velocities measured in the flowfield by PIV.

The net horizontal momentum P_Y and vertical momentum P_Z per unit span through horizontal sides 1 and 3 (Fig. 19) are given by

$$P_Y = \int_{Y_1}^{Y_2} \rho V v \, \mathrm{d}y \qquad P_Z = \int_{Y_1}^{Y_2} \rho V w \, \mathrm{d}y \tag{3}$$

where

$$V = \sqrt{v^2 + w^2} \tag{4}$$

and the mass flow rate per unit span across the sides is given by

$$\dot{m} = \int_{Y_1}^{Y_2} \rho V \, \mathrm{d}y \tag{5}$$

The net horizontal momentum P_Y and vertical momentum P_Z per unit span through vertical sides 2 and 4 are given by

$$P_Y = \int_{Z_1}^{Z_2} \rho V v \, \mathrm{d}z \qquad P_Z = \int_{Z_1}^{Z_2} \rho V w \, \mathrm{d}z \tag{6}$$

The horizontal T_Y and vertical T_Z components of thrust per unit span are then given by

$$\begin{aligned} T_Y &= (P_{Y_3} - P_{Y_1}) + (P_{Y_4} - P_{Y_2}) \\ T_Z &= (P_{Z_3} - P_{Z_1}) + (P_{Z_4} - P_{Z_2}) \end{aligned} \tag{7}$$

respectively, where P_{Z_i} and P_{Y_i} denote the momentum of the fluid per unit span through the ith side, in the Z and Y directions, respectively.

However, this calculation gives only the thrust produced per unit length of the blade at the midspan location, because the PIV measurements were only made at 50% blade span. To obtain the total thrust produced by the rotor, an elliptical lift distribution was assumed along the blade span.

The vertical, sideward, and resultant thrust values computed using the PIV agreed within 15% of the values obtained from the balance measurements.

Wake Integration and Profile Drag

The momentum deficit approach can be used to estimate the sectional drag by comparing the momentum upstream and downstream of the blade section. By using the continuity equation, the equation for the drag is given by [28]

$$D = \frac{1}{2}\rho \int_{-\infty}^{\infty} U_{T_2}(U_{T_1} - U_{T_2}) \, \mathrm{d}s \tag{8}$$

where the subscripts 1 and 2 denote the upstream and downstream locations relative to the blade section, respectively. Here, the quantity $U_{T_1} - U_{T_2}$ is the decrease in flow velocity, which when multiplied by the mass flux ρU_{T_2} gives the decrement in momentum per unit time in the drag direction.

Figure 20 shows the reduction in the flow velocity behind the rotor blade that was obtained from the PIV measurements for the 0° azimuthal location. The coefficient of drag (c_d) for the blade section computed at the 0° azimuthal location (blade pitch angle of 40°) was 0.09, which is a typical value at these Reynolds numbers at such high angles of attack [29].

Comparison of Cyclorotors with Other Hovering Concepts

Figure 21 shows the values of power loading versus equivalent disk loading for cycloidal microrotors, conventional microrotors, large helicopters, as well as biological flyers [28]. Notice that both axes have logarithmic scales. The momentum theory can be used at all the scales to obtain the overall performance of any hovering concept, because it gives theoretical ideal hovering limit. Momentum theory can be expressed using [30]

$$\mathrm{PL} = \frac{\sqrt{2\rho}\mathrm{FM}}{\sqrt{\mathrm{DL}}} \tag{9}$$

The disk loading for the cyclorotor is obtained using the rectangular projected area of the rotor A. It is interesting to note that all the measurements made for the cycloidal microrotors fall consistently on the power loading versus disk loading line for a figure of merit of 0.4 (Fig. 21). However, it can also be seen that conventional microrotors can achieve figure-of-merit values between 0.4 and 0.6 at the same disk loading. One reason for this could be the lack of camber on cyclorotor blades, because camber plays a major role in improving the performance of rotor blades at low Reynolds numbers. However, cyclorotor blades cannot use camber, because they have to operate at both positive and negative angles of attack. Other reasons for lower efficiency of the present cyclorotor could be the rotational losses inside the rotor and the interference between the upper and lower halves of the rotor.

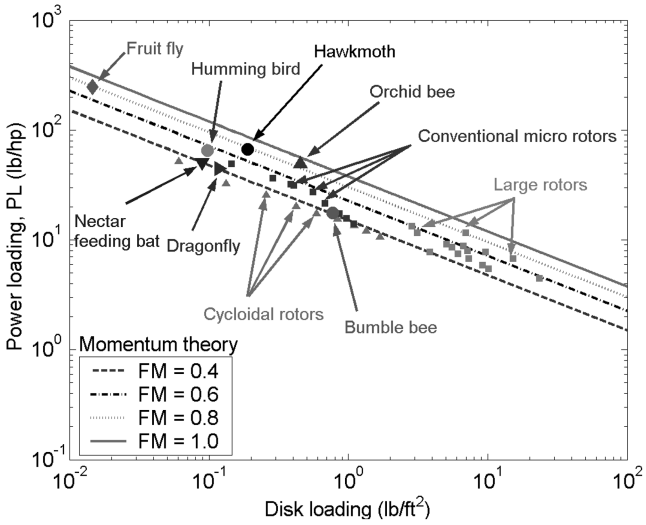

Fig. 21 Power loading versus effective disk loading at different scales.

Clearly there is scope for further improvements in cyclorotor performance through the optimization of blade airfoil section and blade kinematics, such as by having an asymmetric blade pitching (different pitch angle variation at the top and bottom halves of the blade trajectory), varying the blade pitching axis location, etc.

Conclusions

This work has focused on optimizing the performance of a microscale cyclorotor. Four cyclorotors with two-, three-, four-, and five-blades and variable blade pitching amplitudes were built for the experiments. The following are the specific conclusions derived from the study:

1) Power loading (and hence rotor efficiency) increases with increasing number of blades (i.e., increasing rotor solidity) despite the fact that profile power increases with solidity. This is because a rotor system with a higher solidity generates the same thrust at a lower rotational speed compared to a rotor with a lower solidity. The associated reduction in profile power due to the operation at a lower rotational speed outweighs the increase in profile power due to increase in solidity. This trend remained consistent across a wide range of blade pitching amplitudes.

2) Operating the cyclorotor at higher pitching amplitude resulted in improved performance, and this performance seemed independent of the number of blades being used. The optimum cyclorotor configuration from the present study was a five-bladed rotor operating at a pitching amplitude of 40°.

3) A momentum balance performed using the flowfield measurements helped to quantify the vertical and sideward forces produced by the cyclorotor. The estimated momentum values showed good agreement with the force measurements made using load balance. The drag coefficient of the blades was also computed using the momentum deficit approach, and the computed C_d values correlated well with the typical airfoil values for these low Reynolds numbers.

4) The PIV measurements showed that there are significant rotational flows inside the rotor cage, which coupled with the influence of the upper wake on the lower half of the rotor may be the reason for the relatively low efficiency of a cyclorotor. In addition to mitigating these losses, blade camber and optimization of cyclorotor blade kinematics such as asymmetric blade pitching, variation of blade pitching axis location, etc., may further improve the performance of the cyclorotor.

Acknowledgments

This research was jointly supported by the Multidisciplinary University Research Initiative (MURI) grant W911NF0410176 from the U.S. Army Research Office with Tom Doligalski as Technical Monitor and the Army's Micro Autonomous Systems and Technology, Collaborative Technology Alliance, Center for Microsystem Mechanics with Joseph Mait as Technical Monitor. The authors would like to acknowledge Bradley Johnson for his contributions in the particle image velocimetry part of this work and Tejaswi Jarugumilli for his help in building the cyclorotors. The assistance of J. Gordon Leishman for his help in the research and in editing the manuscript is gratefully acknowledged.

References

[1] Ifju, P. G., Jenkins, D. A., Ettinger, S., Lian, Y., Shyy, W., and Waszak, M. R., "Flexible-Wing-Based Micro Air Vehicles," AIAA 40th Aerospace Sciences Meeting and Exhibit, AIAA Paper 2002-705, Reno, NV, Jan. 2002.

[2] Peterson, B., Erath, B., Henry, K., Lyon, M., Walker, B., Powell, N., et al. "Development of a Micro Air Vehicle for Maximum Endurance and Minimum Size," AIAA 41st Aerospace Sciences Meeting and Exhibit, AIAA Paper 2003-416, Reno, NV, Jan. 2003.

[3] Brion, V., Aki, M., and Shkarayev, S., "Numerical Simulation of Low Reynolds Number Flows Around Micro Air Vehicles and Comparison Against Wind Tunnel Data," AIAA 24th Applied Aerodynamics Conference Proceedings, AIAA Paper 2006-3864, San Francisco, June 2006.

[4] Grasmeyer, J. M., and Keennon, M. T., "Development of the Black Widow Micro Air Vehicle," AIAA 39th Aerospace Sciences Meeting and Exhibit, AIAA Paper 2001-0127, Reno, NV, Jan. 2001.

[5] Keenon, M. T., and Grasmeyer, J. M., "Development of the Black Widow and Microbat MAVs and a Vision of the Future of MAV Design," AIAA/ICAS International Air and Space Symposium and Exposition, The Next 100 Years, AIAA Paper 2003-2901, Dayton, OH, July 2003.

[6] Pines, D., and Bohorquez, F., "Challenges Facing Future Micro-Air-Vehicle Development," *Journal of Aircraft*, Vol. 43, No. 2, March–April 2006, pp. 290–305. doi:10.2514/1.4922

[7] Hein, B., and Chopra, I., "Hover Performance of a Micro Air Vehicle: Rotors at Low Reynolds Number," *Journal of the American Helicopter Society*, Vol. 52, No. 3, July 2007, pp. 254–262. doi:10.4050/JAHS.52.254

[8] Kim, S. J., Yun, C. Y., Kim, D., Yoon, Y., and Park, I., "Design and Performance Tests of Cycloidal Propulsion Systems," 44th AIAA/ASME/ASCE/AHS Structures, Structural Dynamics, and Materials Conference, Norfolk, VA, AIAA Paper 2003-1786, April 2003.

[9] Hwang, I. S., Hwang, C. P., Min, S. Y., Jeong, I. O., Lee, C. H., Lee, Y. H., and Kim, S. J., "Design and Testing of VTOL UAV Cyclocopter with 4 Rotors," *Proceedings of the 62nd Annual Forum of the American Helicopter Society*, AHS International, Alexandria, VA, 2006, pp. 2109–2115.

[10] Hwang, I. S., Hwang, C. S., and Kim, S. J., "Structural Design of Cyclocopter Blade System," AIAA/ASME/ASCE/AHS/ASC Structures, Structural Dynamics and Materials Conference, Austin, TX, AIAA Paper 2005-2020, April 2005.

[11] Kim, S. J., Hwang, I. S., Lee, H. Y., and Jung, J. S., "Design and Development of Unmanned VTOL Cyclocopter," *Symposium on Aerospace Science and Technology*, NC, Aug. 2004.

[12] Wheatley, J. B., and Windler, R., "Wind-Tunnel Tests of a Cyclogiro Rotor," NACA TN 528, May 1935.

[13] Wheatley, J., "Simplified Aerodynamic Analysis of the Cyclogiro Rotating-Wing System," NACA TR 467, Aug. 1933.

[14] Kirsten, F. K., "Cycloidal Propulsion Applied to Aircraft," *Transactions of the American Society of Mechanical Engineers*, Vol. 50, No. AER-50-12, 1928, pp. 25–47.

[15] Boschma, J. H., "Modern Aviation Applications for Cycloidal Propulsion," AIAA Aircraft, Technology Integration, and Operations Forum, Los Angeles, AIAA Paper 2001-5267, Oct. 2001.

[16] Gibbens, R., "Improvements in Airship Control using Vertical Axis Propellers," AIAA 3rd Annual Aviation Technology, Integration, and Operations Tech, AIAA Paper 2003-6853, Nov. 2003.

[17] Gibbens, R., Boschma, J., and Sullivan, C., "Construction and Testing of a New Aircraft Cycloidal Propeller," 13th AIAA Lighter-Than-Air Systems Technology Conference, Norfolk, VA, AIAA Paper 1999-3906, June 1999.

[18] McNabb, M., "Development of a Cycloidal Propulsion Computer Model and Comparison with Experiment," M.S. Thesis, Mississippi State Univ., Mississippi State, MS, Dec. 2001.

[19] Nagler, B., "Improvements in Flying Machines Employing Rotating Wing Systems," U.K. Patent Number 280849, Nov. 1926.

[20] Iosilevskii, G., and Levy, Y., "Experimental and Numerical Study of Cyclogiro Aerodynamics," *AIAA Journal*, Vol. 44, No. 12, 2006,

pp. 2866–2870.
doi:10.2514/1.8227

[21] Higashi, Y., Tanaka, K., Emaru, T., and Wang, H. O., "Development of a Cyclogyro-Based Flying Robot with Variable Attack Angle Mechanisms," *IEEE/RSJ International Conference Proceedings on Intelligent Robots and Systems*, Beijing, Oct. 2006, pp. 3261–3266.

[22] Yu, H., Bin, L. K., and Rong, H. W., "The Research on the Performance of Cyclogyro," AIAA 6th Aviation Technology, Integration and Operations Conference Proceedings, AIAA Paper 2006-7704, Wichita, KS, Sept. 2006.

[23] Benedict, M., Ramasamy, M., Chopra, I., and Leishman, J. G., "Performance of a Cycloidal Rotor Concept for Micro Air Vehicle Applications," *Journal of the American Helicopter Society*, Vol. 55, No. 2, April 2010, Paper 022002.
doi:10.4050/JAHS.55.022002

[24] Benedict, M., Sirohi, J., and Chopra, I., "Design and Testing of a Cycloidal Rotor MAV," *Proceedings of the American Helicopter Society International Specialists' Meeting on Unmanned Rotorcraft*, Chandler, AZ, Jan. 2007.

[25] Sirohi, J., Parsons, E., and Chopra, I., "Hover Performance of a Cycloidal Rotor for a Micro Air Vehicle," *Journal of the American Helicopter Society*, Vol. 52, No. 3, July 2007, pp. 263–279.
doi:10.4050/JAHS.52.263

[26] Scarano, F., "Iterative Image Deformation Methods in PIV," *Measurement Science and Technology*, Vol. 13, 2002, pp. R1–R19.
doi:10.1088/0957-0233/13/1/201

[27] Ramasamy, M., and Leishman, J. G., "Benchmarking Particle Image Velocimetry with Laser Doppler Velocimetry for Rotor Wake Measurements," *AIAA Journal*, Vol. 45, No. 11, Nov. 2007, pp. 2622–2633.
doi:10.2514/1.28130

[28] Ramasamy, M., Johnson, B., and Leishman, J. G., "Understanding the Aerodynamic Efficiency of a Hovering Micro-Rotor," *Journal of the American Helicopter Society*, Vol. 53, No. 4, Oct. 2008, pp. 412–428.
doi:10.4050/JAHS.53.412

[29] Laitone, E. V., "Wind Tunnel Tests of Wings at Reynolds Numbers Below 70,000," *Experiments in Fluids*, Vol. 23, 1997, pp. 405–409.
doi:10.1007/s003480050128

[30] Leishman, J. G., *Principles of Helicopter Aerodynamics*, Cambridge Univ. Press, New York, 2000, chap. 2, pp. 378–382.